Editors' Suggestion

Operation of the P̄ANDA cluster-jet target with the HESR stochastic cooling at COSY

P. Brand[1,*] D. Bonaventura,[1] H. Eick,[1] R. Gebel,[2,3] F. Goldenbaum,[2] V. Hejny,[2]
J. Hetzel,[2,3] V. Kamerdzhiev,[2,3] C. Mannweiler,[1] D. Prasuhn,[2] J. Ritman,[2,3,4]
N. Shurkhno,[2,3] R. Stassen,[2] H. Stockhorst,[2] S. Vestrick,[1] M. Weide,[1] and A. Khoukaz[1]

(P̄ANDA Collaboration)

[1]*Institut für Kernphysik, Universität Münster, 48149, Münster, Germany*
[2]*Institut für Kernphysik, Forschungszentrum Jülich GmbH, 52428, Jülich, Germany*
[3]*GSI Helmholtzzentrum für Schwerionenforschung GmbH, 64291, Darmstadt, Germany*
[4]*Institut für Experimentalphysik I, Ruhr-Universität Bochum, 44801, Bochum, Germany*

The P̄ANDA experiment at the High Energy Storage Ring (HESR) of the Facility for Antiproton and Ion Research (FAIR) in Darmstadt, Germany, will be a unique setup to study the strong interaction in antiproton-proton collisions. The combination of a windowless cluster-jet target and a high-intensity antiproton beam, cooled by stochastic cooling down to momentum spreads of 4×10^{-5} in the presence of the target, is ideal to study, e.g., the line shape of exotic candidates in the charmonium spectrum, such as the $\chi_{c1}(3872)$. For first studies on the performance of the cluster-jet target and the stochastic cooling, both were installed at the COoler SYnchrotron (COSY) at the Forschungszentrum Jülich, Germany. Detailed studies on the beam quality for different target settings with different densities were performed and will be presented in this paper. The results show that the cluster-jet target is able to provide the required hydrogen target thickness of more than 2×10^{15} atoms/cm^2 for the P̄ANDA experiment and that the stochastic cooling is able to efficiently cool the beam in presence of such a target thickness, although the system is not yet complete compared to the setup foreseen for the HESR. The presented results strengthen the theoretical understanding of the beam-target interaction and stochastic cooling performance and will provide important input for operation later at the HESR.

I. INTRODUCTION

The new Facility for Antiproton and Ion Research (FAIR) in Darmstadt, Germany, is currently under construction as an extension of the existing accelerator complex of the GSI Helmholtzzentrum für Schwerionenforschung GmbH. Its antiproton branch will provide a unique, high-intensity antiproton beam for the P̄ANDA experiment, which is one of the four major experiments at FAIR. 2.5×10^{13} protons with 29 GeV from the SIS100 will collide every 10 s with a solid target [1], producing about 5×10^8 antiprotons each time [2]. The antiprotons will be extracted via a magnetic horn [1] and collected with an energy of 3 GeV in the Collector Ring, where they are cooled by stochastic cooling from a momentum spread (2σ) of $\Delta p/p = 3\%$ at injection down to 0.1% [3]. These are then guided into the High Energy Storage Ring (HESR), where the antiprotons can be accelerated or decelerated to the desired momentum in the range from 1.5 to 15 GeV/c [4]. At one straight section of the HESR, the P̄ANDA experiment will be located, where the antiprotons collide with protons from a cluster-jet target with a design target thickness of 4.5×10^{15} atoms/cm^2 [5]. This target will cause beam heating that would result in a fast loss of antiprotons. Therefore, the antiproton beam will be cooled by a dedicated stochastic cooling system. This system allows reducing the momentum spread (1σ) of the antiprotons down to $\sigma_p/p = 4 \times 10^{-5}$ in the high resolution (HR) mode of the HESR with 10^{10} stored antiprotons and a maximum momentum of 8.9 GeV/c. In the high luminosity (HL) mode, which would require an additional accumulator ring to increase the number of stored antiprotons to 10^{11}, the momentum spread can be reduced to $\sigma_p/p = 1 \times 10^{-4}$ with a maximum momentum of 15 GeV/c [6].

*Contact author: philipp.brand@uni-muenster.de

This unique combination of an intense and cooled antiproton beam and a windowless cluster-jet target enables the large physics program of the $\bar{\text{P}}$ANDA experiment, which will study nuclear structure and hypernuclear physics and will have a major focus on hadron spectroscopy in both the charmonium and light quark sectors [7]. Here, the nature of antiproton-proton annihilation allows for direct production of states without restriction to $J^{PC} = 1^{--}$, which would be the case for electron-positron annihilation. This enables precise studies with high statistics of exotic candidates, such as $\chi_{c1}(3872)$, which is located at the $D\bar{D}^*$ threshold with a width of only 1.19(21) MeV [8] and is supposed to be a loosely bound $D^0\bar{D}^{*0}$ state; however, a virtual scattering state is possible, which would result in a slightly different line shape. With the precise antiproton beam, $\bar{\text{P}}$ANDA will be able to accurately measure the state's line shape to unravel its nature via the resonance energy scan technique [9]. In this technique, the beam energy is slowly increased from values below the production threshold of the resonance to values above it. The line shape of the resonance is then reconstructed from the measured rate at the different center-of-mass energies, which is a convolution of the state's line shape and the energy spread of the antiproton beam. This method allows for a more precise measurement of the line shape than would be possible through classical reconstruction of the line shape via the invariant mass of the decay products. The resonance scan technique requires a very small and constant momentum spread of the antiproton beam, which is only possible with the stochastic cooling system at the HESR.

The achievable resolution of such a measurement depends on the performance of the stochastic cooling when operating it in combination with a target that causes beam heating. Therefore, the performance of the $\bar{\text{P}}$ANDA cluster-jet target and stochastic cooling has been studied at the COoler SYnchrotron (COSY) at the Forschungszentrum Jülich, Germany, with a focus on the dependence of the reached momentum spread on target thickness and beam intensity.

II. THE $\bar{\text{P}}$ANDA CLUSTER-JET TARGET

The $\bar{\text{P}}$ANDA experiment will be a fixed-target experiment consisting of two parts. Surrounding the interaction point, the target spectrometer with several detection systems for tracking, calorimetry, and particle identification embedded into a superconducting solenoid magnet will be located. Particles with a forward boost will instead be detected inside the forward spectrometer that makes use of a dipole magnet and similar detection systems as the target spectrometer. As target material, mainly hydrogen is foreseen, which will be realized by the powerful $\bar{\text{P}}$ANDA cluster-jet target [10]. Such cluster-jet targets [11–17] have routinely been used in other internal experiments such as COSY-11 or ANKE [18–20] as their windowless design is ideal for such a setup. Nevertheless, the design of the $\bar{\text{P}}$ANDA target spectrometer with its solenoid only allows an installation of the target on top of the solenoid at a large
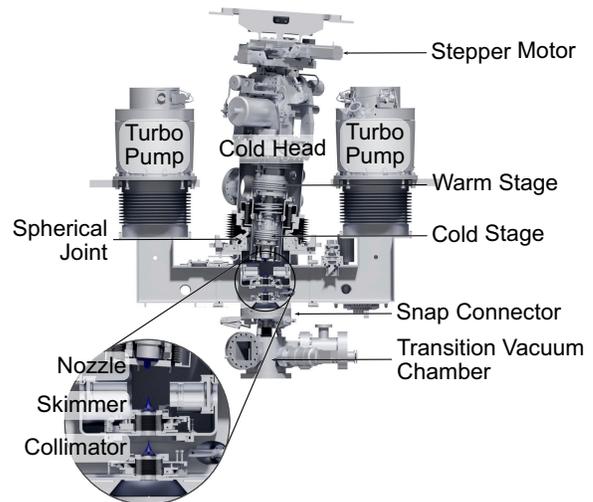

FIG. 1. CAD drawing of the $\bar{\text{P}}$ANDA cluster-jet target source. Ultrapure hydrogen gas enters the target and is cooled within the copper pipe windings around the warm and cold stages of the two-stage cold head. The gas is pressed under high pressure of up to 20 bar and temperatures down to 20 K through a convergent-divergent de Laval nozzle. The resulting cluster jet is separated from residual gas and shaped by a circular skimmer and a rectangular collimator. Gas remaining inside the skimmer or collimator chamber is pumped away by a powerful pumping station and two turbomolecular pumps.

distance of 2.25 m to the interaction point, while the required target thickness of up to 4.5×10^{15} atoms/cm² has never been reached at such a distance before.

To fulfill these requirements, a new powerful cluster-jet target has been developed that has proven to constantly reach target thicknesses of more than 1×10^{15} atoms/cm². The main part of the target is its source, as shown in Fig. 1, which will be installed on top of the $\bar{\text{P}}$ANDA solenoid. Ultrapure hydrogen gas (impurity $< 10^{-9}$) enters the target with a pressure of up to 20 bar and is guided through copper windings around the two stages of a two-stage cold head, i.e., the warm and cold stages. To minimize the heat conductance with the outer walls, these two stages are surrounded by the insulation vacuum chamber. This way, final temperatures down to 20 K can be reached, allowing target operation with hydrogen in the gaseous, supercritical, and liquid regime with completely different properties, such as cluster size distribution or the cluster velocity [21]. The cooled hydrogen then leaves the target through a convergent-divergent de Laval nozzle with a diameter of 28 μm in its narrowest inner part. The fluid expands into vacuum and creates a supersonic cluster jet with cluster sizes up to several micrometers when using liquid hydrogen [22]. Behind the nozzle exit, a conical orifice with a circular opening,—the skimmer—is mounted. It extracts a small part of the cluster jet and separates it from the residual gas. A powerful pumping station, which houses two stages of roots pumps with a total pumping speed of more than 7000 m³/h,

pumps away the gas that is not passing the skimmer and that remains in the skimmer chamber [5]. The part of the jet that passes through the skimmer enters the collimator chamber, where another orifice is mounted. This collimator has a rectangular opening and creates the final shape of the cluster jet. Gas remaining in the collimator chamber is pumped away by two turbomolecular pumps. To achieve the highest thickness, skimmer and collimator are mounted on movable cross tables and the whole target source can be tilted, so that a very dense part of the jet can be extracted. With this method, a well-defined cluster jet is prepared that can travel the distance of 2.25 m from the nozzle down to the interaction point in the center of the P̄ANDA solenoid. From there, it continues roughly the same distance to the other side of the solenoid, where a three-stage beam dump equipped with seven turbomolecular pumps removes most of the gas from the vacuum system.

III. THE STOCHASTIC COOLING SYSTEM FOR THE HESR

Stochastic cooling [23] is a commonly used [24–28] method to create precise particle beams and to compensating for beam heating effects, e.g., by internal targets. The stochastic cooling system for the HESR consists of independent kicker and pickup tanks for longitudinal, horizontal, and vertical cooling. This system will reduce the beam size and the momentum spread, and, together with a barrier bucket cavity, it will compensate beam heating effects induced by the P̄ANDA cluster-jet target. Each tank consists of ring-slot couplers with 8 electrodes. They are mounted into stacks of 16 rings, as shown in Fig. 2 and finally four stacks will be mounted into each tank. For increasing the signal-to-noise ratio, the inner structure is cooled down by two cryogenic cold heads to temperatures below 20 K. The system will operate in the frequency range of 2 to 4 GHz and

for longitudinal cooling the time-of-flight method as well as the filter method are available. The first pickup tank designed for the HESR was installed in winter 2015/2016, followed by the first kicker in summer 2016, and they were finally commissioned in 2017 [29].

IV. EXPERIMENTAL SETUP AT COSY

The P̄ANDA cluster-jet target and also parts of the stochastic cooling for the HESR are installed at COSY (see Fig. 3), which can deliver proton and deuteron beams with momenta up to 3.7 GeV/c [20]. They are injected from the cyclotron JULIC and then accelerated to their final momenta. The accelerated particles can be used in internal experiments such as the former ANKE or WASA experiments or can be extracted into the external areas. At COSY, a barrier bucket cavity is installed that was used during the beam times described in this work to compensate beam energy losses due to beam-target interaction. Furthermore, a kicker and a pickup tank of the stochastic cooling system for the HESR are available at COSY, which reduce the momentum spread and can compensate for beam heating effects induced by the cluster-jet target. The momentum spread can then be studied by an independent pickup tank working in a different frequency regime. The effect of transversal cooling is monitored by two ionization profile monitors (IPM) that measure the horizontal and the vertical beam profiles.

FIG. 2. Ring-slot coupler stacks for the HESR stochastic cooling system. The smaller stacks on the right are shown without and with combiner boards. Two of them are then combined to the final stack size on the left [29].
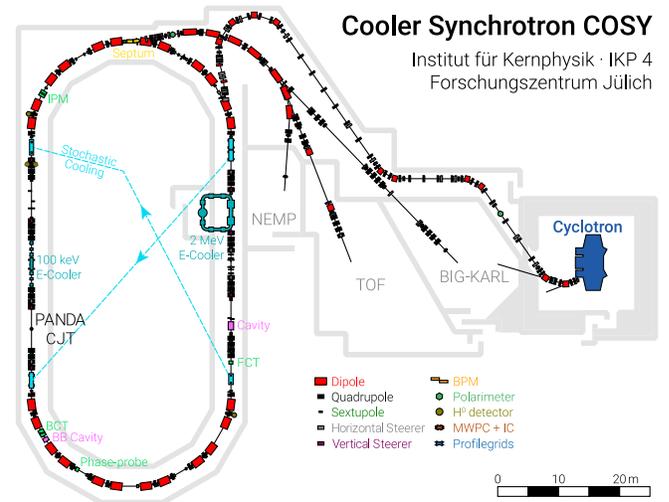

FIG. 3. Plan of the COoler SYnchrotron (COSY). Proton and deuteron beams can be injected from the cyclotron JULIC and are then accelerated to their final momenta of up to 3.7 GeV/c. This beam can then be used by internal experiments or it can be extracted and guided toward the external experimental areas. The P̄ANDA cluster-jet target is installed at the former WASA experimental area on the left side. Additionally, the stochastic cooling system for the HESR is installed at COSY with the pickup tank on the lower right of the ring and the kicker on the upper left.
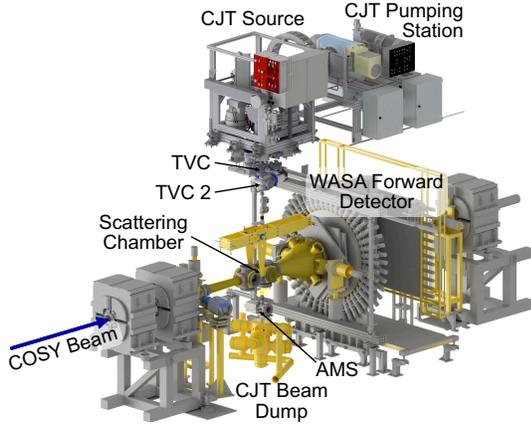
FIG. 4. CAD drawing of the $\bar{\text{P}}$ANDA cluster-jet target (CJT) setup at COSY. The target source is installed on top of the concrete ceiling of the COSY tunnel at the location of the former WASA experiment. The WASA central detector was removed to make space for a larger scattering chamber, an absolute thickness monitor system (AMS), and the target beam dump. While the distance between target source and the interaction point is in $\bar{\text{P}}$ANDA geometry, the distance to the beam dump is reduced due to space constraints. Downstream of the interaction point, the WASA forward detector is located and still operational. It was used to find the perfect overlap of the COSY beam and the target by monitoring the rate.

The target was installed at COSY in summer 2018 at the experimental area of the former WASA experiment [30], as shown in Fig. 4. The cluster-jet target source and its pumping station are placed on top of the concrete ceiling of the COSY tunnel, so that the distance between the nozzle and the COSY beam line is 2.25 m, as it will be later at $\bar{\text{P}}$ANDA. Due to spatial constraints underneath the beam line, the beam dump is mounted much closer to the interaction point. Furthermore, due to the removal of the WASA forward detector, space for a larger interaction chamber equipped with a turbomolecular pump and pressure gauges is available and also an absolute thickness monitor system (AMS) is installed between the interaction point and the beam dump. Later at $\bar{\text{P}}$ANDA, there will be no space due to the $\bar{\text{P}}$ANDA detector with its solenoid magnet, so that an updated beam dump will be used that has space for monitor systems such as the AMS.

The AMS is shown in Fig. 5 and consists of two perpendicular rods, which are scanned one after the other through the cluster jet to acquire the beam profiles in two dimensions. Clusters hitting the rod break up and create a pressure increase that is measured by a pressure gauge as a function of the rod position. From the pressure increase, the cluster velocity, and the known pumping speed, the thickness of the cluster jet can be calculated [31]. For this purpose, the pressure profiles can be fitted by

$$p(x) = p_{0,a} b_z \int_{x-d/2}^{x+d/2} \tilde{\rho}_x(x') \mathrm{d}x' + p_{\text{back}} \qquad (1)$$
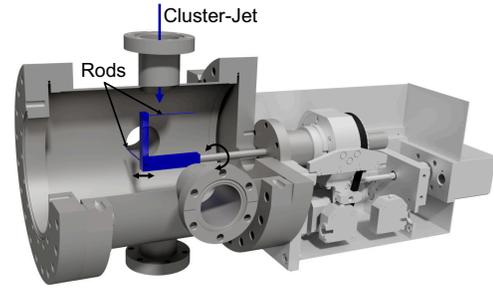

FIG. 5. CAD drawing of the absolute thickness monitor system (AMS) that is installed at the $\bar{\text{P}}$ANDA cluster-jet target setup at COSY. The two rods scan through the cluster jet one after the other to get beam profiles in two dimensions. Clusters hitting these rods cause a pressure increase that is recorded and that can be converted into an absolute target thickness.

with

$$\tilde{\rho}_x(x) = \frac{1}{2}\left[\text{erf}\left(\frac{x - x_0 + b_x/2}{s}\right) - \text{erf}\left(\frac{x - x_0 - b_x/2}{s}\right)\right], \qquad (2)$$

where $p_{0,a}$ is a scaling parameter, b_z is the cluster-jet width in z direction (accelerator beam direction), $d = 1$ mm is the diameter of the rod, p_{back} is the background pressure, x is the position of the rod, b_x is the beam width in the horizontal direction, and s is a smearing parameter. This function assumes a homogeneous, rectangular cluster jet that is smeared out at its edges by a Gaussian with $s = \sqrt{2}\sigma$ [31]. The target thickness is then given as

$$n_T = 2p_{0,a} \frac{SN_A}{vRT} b_z \text{erf}\left(\frac{b_z}{2s}\right) \qquad (3)$$

with the pumping speed S, the Avogadro number N_A, the velocity of the clusters v, the universal gas constant R, and the temperature $T \approx 293$ K of the gas inside the AMS chamber [31].

The profile with the highest target thickness recorded during the beam times presented in this work is shown in Fig. 6. The target was operated at 23 K and 18 bar resulting in a target thickness of $(3.14 \pm 0.17) \times 10^{15}$ atoms/cm^2, which is close to the maximum target thickness required by the $\bar{\text{P}}$ANDA experiment and which marks a new record density with the $\bar{\text{P}}$ANDA cluster-jet target. A larger value has only been achieved at the Münster prototype target with the same nozzle and a similar target geometry [32]. Unfortunately, this very high target thickness often leads to more unstable operation. As a result, it was not achievable for a long period, during which the accelerator beam was also unavailable, and no data could be recorded at this highest target thickness. Nevertheless, the target ran stably over more than 9 h with a target thickness of still more than 10^{15} atoms/cm^2.
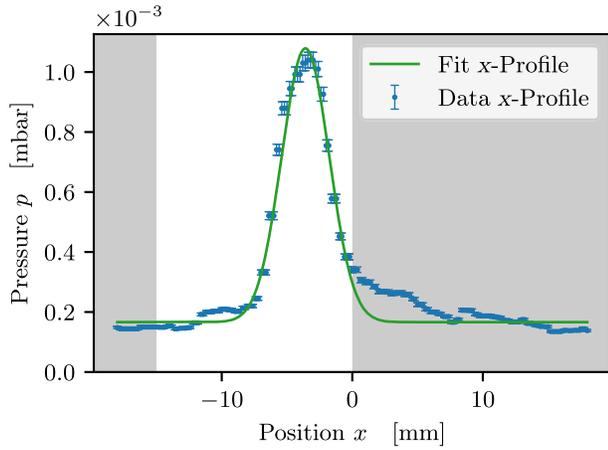
FIG. 6. Target profile recorded with the target operating at 23 K and 18 bar with a record target thickness of $(3.14 \pm 0.17) \times 10^{15}$ atoms/cm^2. The data in the gray area are not included in the fit to avoid the influence of the asymmetric shape.

V. BEAM QUALITY STUDIES

The main focus of the three beam times in 2021, 2022, and 2023 was the study of the achievable beam quality when operating the cluster-jet target under different conditions in combination with stochastic cooling. Therefore, different target conditions resulting in target thicknesses varying over 2 orders of magnitude and different beam intensities were chosen and the achieved momentum spread was measured. The used target settings with the resulting target thickness that were used during the different beam times are shown in Fig. 7. Here, the 2021 beam time is divided into two parts, in May and June, as there was a short break during the data runs and some target settings
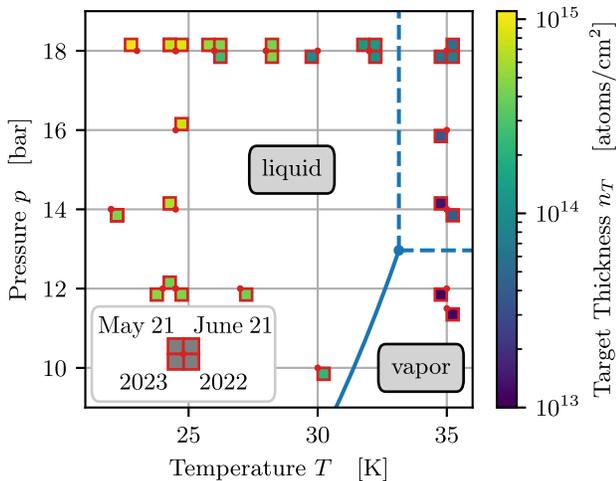

FIG. 7. Target settings with the resulting target thicknesses used during the beam quality measurements in the phase diagram of hydrogen. The solid blue line corresponds to the vapor pressure curve, and the dashed lines mark the region of supercritical hydrogen. The four quadrants correspond to the three beam times with the 2021 beam time divided into two parts in May and June.

were repeated. For comparable results, in every beam time each COSY cycle was structured similarly. After injection and acceleration of the beam, the barrier bucket cavity was activated and the stochastic cooling was turned on without a target beam present to allow for sufficient precooling. After 10 s, the target was turned on by means of a shutter inside the skimmer chamber, which can block the cluster jet and stops it from entering the COSY vacuum system. The cycles then took roughly 5 min before, at the end, the target, the stochastic cooling, and the barrier bucket were turned off in this order. During the cycle, the momentum spread was monitored by the old stochastic cooling pickup of COSY in steps of 1 s, so that the evolution of the momentum spread was recorded.

Such spectra are shown in Fig. 8, which were recorded after 80 s of the cycle with a target thickness of $(1.00 \pm 0.42) \times 10^{15}$ atoms/cm^2 at 23 K and 18 bar and with $(1.32 \pm 0.05) \times 10^{14}$ atoms/cm^2 at 32 K and 18 bar. The first spectrum shows a clear main peak that is slightly asymmetric and a prominent side peak. This effect can be attributed to the large target thickness. The large target
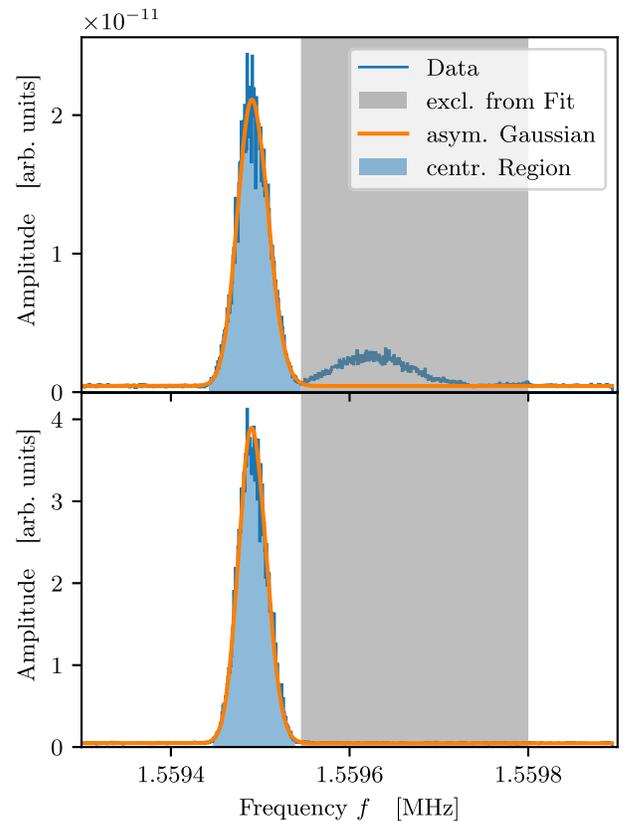

FIG. 8. Recorded Schottky spectra with the target operating at 23 K and 18 bar with a resulting target thickness of $(1.00 \pm 0.42) \times 10^{15}$ atoms/cm^2 (top) and at 32 K and 18 bar with $(1.32 \pm 0.05) \times 10^{14}$ atoms/cm^2 (bottom). In the upper plot, the data show a clear side peak that is excluded (gray area) from the analysis. This cannot be observed at smaller target thickness as shown in the lower plot.

thickness leads to significant energy loss of the beam particles, which cannot be fully compensated by the barrier bucket cavity in combination with the stochastic cooling. As a result, some particles cannot be confined within the bucket and instead form a side peak at lower frequencies. The intensity of this side peak increases with both target thickness and beam intensity. Later at the HESR, the barrier bucket cavity will be optimized, for example, by increasing its potential, so that this effect is not expected. Furthermore, this very prominent side peak is only the most extreme case that occurs when combining a large target thickness with an intense COSY beam. For most other settings with a smaller target thickness this side peak does not occur as shown in the second spectrum. In the following analysis, only the properties of the main peak will be discussed. Therefore, the data in the gray area in Fig. 8 that start at the bucket edge are neglected and an asymmetric Gaussian function

$$g(f) = A \exp\left(-\frac{(f - f_0)^2}{2\sigma(f)^2}\right) + c \tag{4}$$

with

$$\sigma(f) = \begin{cases} \sigma_l & \text{for } f < f_0 \\ \sigma_r & \text{for } f \geq f_0 \end{cases}, \tag{5}$$

including a constant offset c is fitted to the remaining data. With this fit, a central region is determined that is limited on the left by 3σ from the center of the fit, and on the right either by 3σ or by the bucket edge, depending on which of both values is smaller. The variance of the main peak is then calculated as a sum within the central region corrected via integrals over the fit function outside this region:

$$\sigma_f^2 = \frac{1}{n}\left(\sum_{i,\text{central}} (f_i - \bar{f})^2 (S(f_i) - c)\right.$$

$$+ \frac{1}{\Delta f}\int_{-\infty}^{f_l} (f - \bar{f})^2 (g(f) - c)\mathrm{d}f$$

$$\left. + \frac{1}{\Delta f}\int_{f_r}^{\infty} (f - \bar{f})^2 (g(f) - c)\mathrm{d}f\right). \tag{6}$$

The normalization is given as

$$n = \sum_{i,\text{central}} (S(f_i) - c) + \frac{1}{\Delta f}\int_{-\infty}^{f_l} (g(f) - c)\mathrm{d}f$$

$$+ \frac{1}{\Delta f}\int_{f_r}^{\infty} (g(f) - c)\mathrm{d}f. \tag{7}$$

Here, f_l and f_r are the limits of the central region, Δf is the bin width of the recorded Schottky spectrum, and $S(f_i)$ are the data points.

The width of the main peak is then used to calculate the relative momentum spread via

$$\frac{\sigma_p}{p} = \frac{1}{\eta}\frac{\sigma_f}{f} \tag{8}$$

with the phase slip factor

$$\eta = \frac{1}{\gamma^2} - \frac{1}{\gamma_{\text{tr}}^2} = -0.0963 \pm 0.0013 \tag{9}$$

that was measured by variation of the magnetic field of the COSY dipoles leading to a shift of the revolution frequency in the Schottky spectra. The magnetic field was measured via an NMR probe [33].

The measured evolution of the momentum spread within a cycle is shown in Fig. 9 for a target thickness of $(1.32 \pm 0.05) \times 10^{14}$ atoms/cm^2 at 32 K and 18 bar. This shows how the stochastic cooling is able to reduce the momentum spread until it reaches an equilibrium value after roughly 100 s, which is small compared to the cycle times of around 1800 s envisaged later at the HESR. This equilibrium value is extracted by taking the mean value in a 30 s time interval (gray area in Fig. 9) shortly before turning off the target and the stochastic cooling at the end of the cycle. This value is extracted for every combination of the target thickness n_T and the number N_p of stored protons in COSY and by this the dependence of the momentum spread in the equilibrium on both quantities can be studied, which is expected to follow [34,35]

$$\left(\frac{\sigma_p}{p_0}\right)_{\text{eq}} \propto (n_T N_p)^{1/3}. \tag{10}$$

In the following, the data will be described with a more general ansatz that allows for separate power laws for the
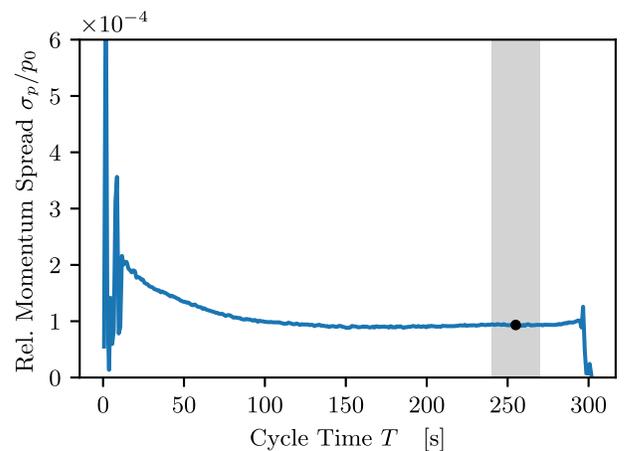

FIG. 9. Relative momentum spread evolution during a cycle with a target thickness of $(1.32 \pm 0.05) \times 10^{14}$ atoms/cm^2 at 32 K and 18 bar. The equilibrium value is extracted as mean at the end of the cycle (gray area).

momentum spread dependence on the target thickness and accelerator beam intensity:

$$\left(\frac{\sigma_p}{p_0}\right)_{eq} \propto (M_1 n_T^{p_1} + A_1)(M_2 N_p^{p_2} + A_2). \quad (11)$$

To minimize correlations in the applied fits, this function is reduced to

$$g(n_T, N_p) = a(m_1 n_T^{p_1} + 1)(m_2 N_p^{p_2} + 1). \quad (12)$$

The data of all beam times are shown in Fig. 10 with the data points from the 2021 and 2022 beam times being scaled by $1/s_{bt}$. This scaling factor is necessary due to the slightly different settings of the stochastic cooling, the accelerator beam, and the target that were
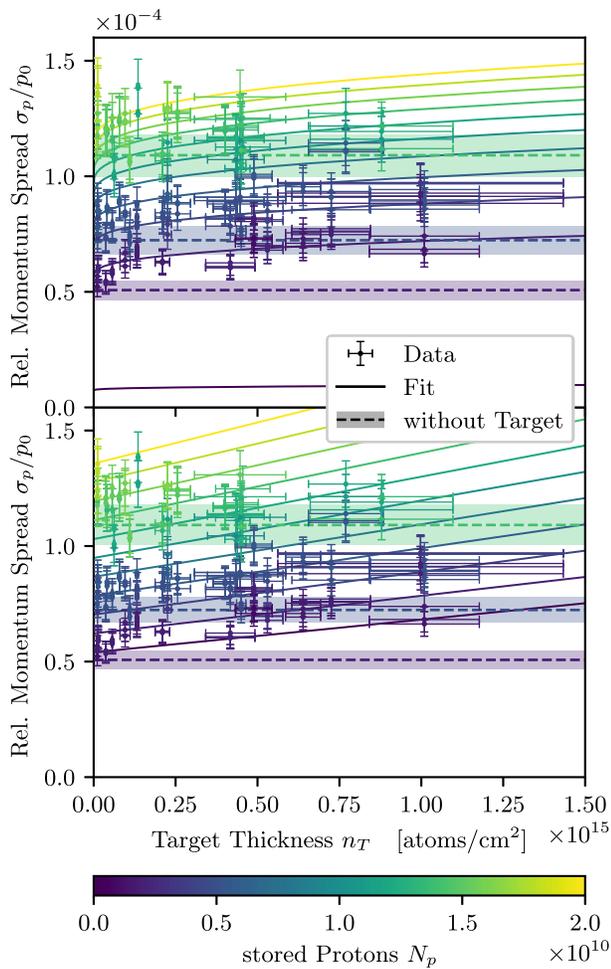

FIG. 10.   Equilibrium momentum spread as a function of the target thickness and the number of stored particles in COSY with a power law fit [Eq. (12)] with $p_1 = p_2 = 1/3$ (top) and $p_1 = p_2 = 1$ (bottom). The data of the beam times in 2021 and 2022 are scaled by $1/s_{bt}$, which is determined by the fit. Additional data taken without a target are shown as horizontal lines. The additional uncertainty [Eq. (16)] is included in the vertical error bars and error bands.

used during the different beam times. These differences cause a noticeable shift between the results of the three beam times, but they should not affect the overall dependence on target thickness and beam intensity. To make the data of all beam times comparable, an additional scaling factor was applied to each dataset. It is determined by fitting the data with the function defined in Eq. (12). In this fit, the parameters s_{bt} are treated as free fit parameters, as introduced in Eq. (13), except for the scaling parameter s_{2023}, which is fixed to 1, so that the data from the last beam time serves as reference. The fit is performed with fixed exponents of $p_1 = p_2 = 1/3$ according to the expectations in the upper plot of Fig. 10. For comparison in the lower plot, a linear dependence with $p_1 = p_2 = 1$ is used, which will be discussed later. Therefore,

$$\chi^2 = \sum_{bt,i} \frac{(s_{bt}g(n_{T,i}, N_{p,i}) - y_i)^2}{(\Delta y_i)^2 + (\Delta y_{n_T,i})^2 + (\Delta y_{N_p,i})^2} \quad (13)$$

with

$$\Delta y_{n_T,i} = s_{bt}g_{n_T}(n_{T,i}, N_{p,i})\Delta n_{T,i} \quad (14)$$

and

$$\Delta y_{N_p,i} = s_{bt}g_{N_p}(n_{T,i}, N_{p,i})\Delta N_{p,i} \quad (15)$$

was minimized, where y_i is the equilibrium momentum spread of the data points, $n_{T,i}$ and $N_{p,i}$ are the corresponding target thickness and number of stored particles in COSY, and $g_{n_T} = \partial g/\partial n_T$ and $g_{N_p} = \partial g/\partial N_p$ are the partial derivatives used to include the uncertainties of target thickness and COSY intensity into the fit. Furthermore, it is observed that the data show rather large variations that cannot be explained by the statistical uncertainties. Therefore, the uncertainty

$$(\Delta y_i)^2 = \sigma_{y,i}^2 + (k y_i)^2 \quad (16)$$

consists of the statistical uncertainty $\sigma_{y,i}$ of the data determined from the fluctuation inside the 30 s time interval and an additional uncertainty that reflects the necessity of manually adjusting the stochastic cooling parameters for every new setting. This introduces an uncertainty that cannot be specified. Instead, the parameter k is introduced that is determined by demanding $\chi^2_{red} = 1$. This is achieved with $k = 0.083$, so that an additional uncertainty of 8.3% is needed to describe the data well. This uncertainty is already included in the vertical error bars and error bands in Fig. 10. All the resulting fit parameters are summarized in Table I.

A. Consequences for the P̄ANDA experiment

One of the signatures of the P̄ANDA experiment is the resonance energy scan measurements. The resolution of these is not limited by the resolution of the detector but by the energy spread of the antiproton beam. The measurements at COSY show that a momentum spread below 2×10^{-4} is

TABLE I. Fit results for the relative momentum spread as a function of the target thickness and the number of stored particles.

	$p_1 = p_2 = 1/3$	$p_1 = p_2 = 1$
a	$(7.3 \pm 2.0) \times 10^{-6}$	$(5.40 \pm 0.09) \times 10^{-5}$
m_1 $(1/(\text{at.}/\text{cm}^2)^{p_1})$	$(2.8 \pm 0.4) \times 10^{-6}$	$(2.6 \pm 0.3) \times 10^{-16}$
m_2	$(5.3 \pm 1.6) \times 10^{-3}$	$(7.6 \pm 0.4) \times 10^{-11}$
s_{2021}	1.135 ± 0.020	1.138 ± 0.020
s_{2022}	1.33 ± 0.03	1.37 ± 0.03
k	0.083	0.077

achieved for all settings. This is already quite close to the value expected for the HL mode of $\bar{\text{P}}$ANDA but still about a factor of 4 off from the goal for the HR mode. However, these absolute values are not directly comparable as several parameters such as the phase slip factor η, the revolution frequency, and the beam energy are different at COSY and the HESR, where a momentum spread of $\sigma_p/p = 4 \times 10^{-5}$ is expected for the HR mode [6]. Furthermore, also only a part of the stochastic cooling system for the HESR was in operation at COSY, so that also a larger cooling power is expected. An interesting quantity to observe is how, for example, a variation in the target thickness affects the momentum spread. Therefore, the relative variation of the function $g(n_T, N_p)$ in Eq. (12) as result of the variation of the target thickness is given as

$$\left(\frac{\Delta g}{g}\right)_{n_T} = \frac{1}{g}\frac{\partial g}{\partial n_T}\Delta n_T = \frac{m_1 p_1 n_T^{p_1-1} \Delta n_T}{m_1 n_T^{p_1} + 1}. \quad (17)$$

Taking the two examples already mentioned, a target thickness of $(1.00 \pm 0.42) \times 10^{15}$ atoms/cm^2 at 23 K and 18 bar, which has a variation of 42%, results in a variation of the momentum spread of only $(3.2 \pm 0.4)\%$. At 32 K and 18 bar with $(1.32 \pm 0.05) \times 10^{14}$ atoms/cm^2 the variation would be nearly negligible with $(0.127 \pm 0.014)\%$. This result can be compared to the variation of the momentum spread caused by the beam loss during a cycle due to hadronic interactions. While the function $g(n_T, N_p)$ describes the equilibrium momentum spread, when the stochastic cooling is optimized for the target thickness and beam intensity, the cooling system will not be readjusted during a cycle. However, for a constant target thickness and without readjusting the stochastic cooling, the momentum spread will decrease linearly [35]. Assuming that the stochastic cooling was adjusted for the initial number of stored protons $N_{p,0}$, the momentum spread will follow

$$f(n_T, N_p) = m(N_p - N_{p,0}) + g(n_T, N_p) \quad (18)$$

with the slope

$$m = \frac{\partial g}{\partial N_p}\bigg|_{N_p=N_{p,0}} = a(m_1 n_T^{p_1} + 1)m_2 p_2 N_{p,0}^{p_2-1}. \quad (19)$$

This describes a tangent to the function $g(n_T, N_p)$ at the point $(n_T, N_{p,0})$. The variation of the momentum spread can then be calculated as

$$\begin{aligned}\left(\frac{\Delta f}{f}\right)_{N_p} &= \frac{f(n_T, N_p(T)) - f(n_T, N_{p,0})}{f(n_T, N_{p,0})}\\ &= \frac{m(N_p(T) - N_{p,0})}{g(n_T, N_{p,0})}\\ &= \frac{m_2 p_2 N_{p,0}^{p_2-1}}{m_2 N_{p,0}^{p_2} + 1}(N_p(T) - N_{p,0}) \quad (20)\end{aligned}$$

with the number of initially stored protons $N_{p,0}$ and the number of stored protons $N_p(T)$ at the end of a cycle of length T, which is given by

$$N_P(T) = N_{p,0} \exp\left(-\sigma_{\text{p}\bar{\text{p}}} n_T f_0 T\right) \quad (21)$$

with the total p$\bar{\text{p}}$ cross section $\sigma_{\text{p}\bar{\text{p}}} \approx 100$ mb [8], the target thickness n_T, the revolution frequency f_0, and the cycle time T. Assuming typical numbers for the HESR of $N_{p,0} = 10^{10}$, $f_0 = 0.522$ MHz, and $T = 1800$ s, the variation of the momentum spread due to the beam loss is given as $(-2.75 \pm 0.07)\%$ for a target thickness of 1×10^{15} atoms/cm^2, which is in the same order of magnitude as the variation due to the target thickness. Therefore, even if the variation of the target thickness will be reduced by a more stable operation, the variation of the momentum spread cannot be reduced below the effect of the beam loss. However, the influence of this on the data can be reduced by measuring the momentum spread during the cycle and by correcting for the momentum spread variation in the data analysis. This will ensure that $\bar{\text{P}}$ANDA will be able to deliver precise results with the line shape measurements.

Another important feature that can be extracted from this data is the combination of target thickness and beam intensity that minimizes the momentum spread for a fixed luminosity. This correlation can be calculated by replacing the number of stored particles N_p in Eq. (12) by the luminosity $L = N_p n_T f_0$ and by demanding $\partial g(n_T, L)/\partial n_T = 0$. This results for $p_1 = p_2 = p$ in

$$L(n_{T,\text{opt}}) = f_0\left(\frac{m_1(1-m_2)}{m_2(1-m_1)}\right)^{1/p} n_{T,\text{opt}}^2 \quad (22)$$

and thus

$$\begin{aligned}N_{p,\text{opt}}(n_{T,\text{opt}}) &= \frac{L(n_{T,\text{opt}})}{n_T f_0}\\ &= \left(\frac{m_1(1-m_2)}{m_2(1-m_1)}\right)^{1/p} n_{T,\text{opt}},\end{aligned} \quad (23)$$

which is shown in Fig. 11. When changing to a larger luminosity, the target thickness and beam intensity should both be increased. Only if one quantity reaches its maximum value, as it is assumed in Fig. 11 for the target thickness when
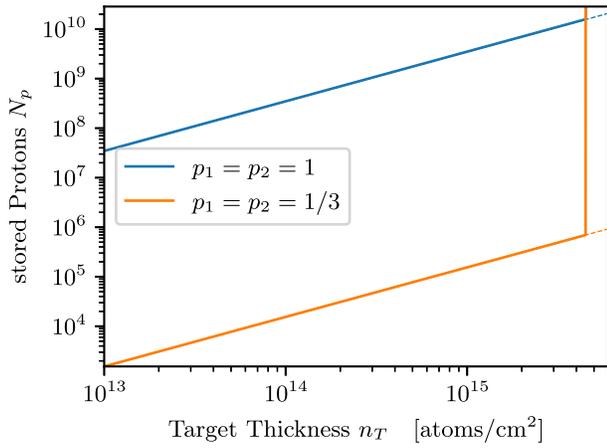
FIG. 11. Optimum combinations of target thickness and beam intensity, which result in the smallest equilibrium momentum spread for that luminosity with $p_1 = p_2 = 1/3$ and $p_1 = p_2 = 1$. Once the target thickness reaches its maximum, which is assumed to be the P̄ANDA design value of 4.5×10^{15} atoms/cm^2, only the beam intensity can be changed (vertical lines). This deviation from the optimum combination (dashed lines) will result in a stronger increase of the momentum spread as shown in Fig. 12.

it reaches the design value of 4.5×10^{15} atoms/cm^2, one should deviate from this relation. However, this leads to a faster increase of the momentum spread as shown in Fig. 12. In case of the fit with $p_1 = p_2 = 1/3$, the maximum target thickness is reached quite fast with a rather small number of stored particles of less than 10^6, so that one would in principle always work with maximum target thickness and then only set the beam intensity according to the demands.
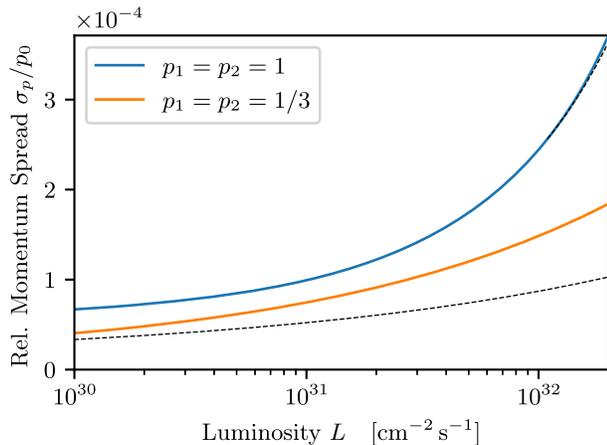

FIG. 12. Momentum spread as a function of the luminosity when operating with the optimum combinations of target thickness and beam intensity. Once the maximum target thickness (4.5×10^{15} atoms/cm^2) is reached, only the beam intensity can be changed, which will result in a stronger increase of the momentum spread and a deviation from the optimum (dashed lines). For $p_1 = p_2 = 1$, this point is reached at a luminosity of approximately 1.1×10^{32} cm^{-2} s^{-1}, while for $p_1 = p_2 = 1/3$, it is already reached at around 4.9×10^{27} cm^{-2} s^{-1}.

When one would instead use a linear dependency with $p_1 = p_2 = 1$, which can also describe the data sufficiently well (see lower plot in Fig. 10) and even results in a slightly smaller additional uncertainty of $k = 0.077$, the maximum target thickness is reached at nearly 2×10^{10} stored particles as shown in Fig. 11. This is already on the order of the maximum intensity at COSY. In this case, both the target setting and the beam intensity should be adjusted when modifying the luminosity. Therefore, this measurement highlights the importance of precise knowledge of the momentum spread dependence on target thickness and beam intensity for the future operation of the HESR and the P̄ANDA experiment.

These results cannot directly be applied to the HESR, as several important parameters for the stochastic cooling performance are different. An overview of these parameters is provided in Table II. The HESR design yields a smaller phase slip factor η, which reduces the efficiency of stochastic cooling. However, the lower revolution frequency at the HESR allows the operation of the stochastic cooling at higher harmonics, partially compensating for the reduced η. At COSY, only one pickup and one kicker tank were available, with two of the four ring-slot coupler stacks used for transverse cooling and one for longitudinal cooling. In contrast, the HESR will employ two pickup tanks, improving the signal-to-noise ratio and reducing noise-related heating. Additionally, two kicker tanks with all four stacks will be used, one for transverse and one for longitudinal cooling. This configuration will further enhance the cooling performance, as at COSY the main amplifiers had to operate at higher gain, leading to operation in saturation. Together with an optimized barrier bucket cavity, these improvements are expected to result in better stochastic cooling performance at the HESR, although the precise impact of these changes cannot be easily quantified. Therefore, such a study should be repeated to find the best operation parameters for the HESR, and it is especially important to reduce the uncertainties, e.g., by improving the stability of the P̄ANDA cluster-jet target, so that the parameters of the fit function can be determined more precisely and the two models used here can be distinguished better.

TABLE II. Comparison of important parameters of the COSY configuration during these measurements and of the planned configuration of the HESR impacting the results of the stochastic cooling performance.

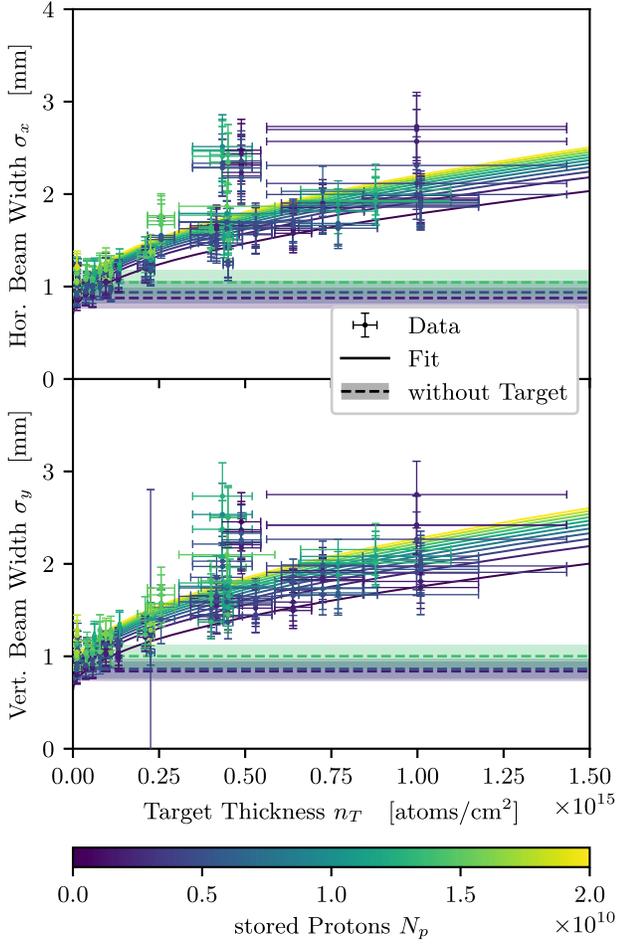|	COSY	HESR
Momentum (GeV/c)	3.0	1.5–15 [4]
Revolution frequency (MHz)	1.559496	0.442–0.522 [4]
Stored (anti)protons	$<2 \times 10^{10}$	$<1 \times 10^{11}$ [4]
Transition energy γ_{tr}	2322 ± 0.017 [33]	6–30 [36]
Pickup tanks	1	2
Kicker tanks	1 (3 of 4 stacks)	2

FIG. 13. Equilibrium horizontal (top) and vertical (bottom) beam widths as a function of the target thickness and the number of stored particles in COSY with a power law fit [Eq. (12)] with $p_1 = p_2 = 1/2$. The data of the beam times in 2021 and 2022 are scaled by $1/s_{bt}$, which is determined by the fit. Additional data taken without a target are shown as horizontal lines. The additional uncertainty [Eq. (16)] is included in the vertical error bars and error bands.

B. Beam width study

While the main focus of the presented studies was on the momentum spread, the beam width was also monitored during the cycles using two ionization profile monitors (IPM) installed at COSY [37]. These devices allow for nondestructive measurement of the horizontal and vertical beam profiles, making it possible to monitor the effect of transverse cooling. The extracted width does not correspond to the width at the target position due to different values of the β-function at the IPM and target position. Therefore, the measured width at the IPM position is scaled to the target position using the β-functions at both locations.

The measured horizontal and vertical beam widths at the target position for different target settings and beam intensities are shown in Fig. 13. This data were analyzed using the same method as described above for the

TABLE III. Fit results for the horizontal and vertical beam widths at the target position as a function of the target thickness and the number of stored particles with $p_1 = p_2 = 1/2$.

	Horizontal	Vertical
a (mm)	0.69 ± 0.04	0.63 ± 0.03
$m_1 \left(1/(\text{at.}/\text{cm}^2)^{p_1}\right)$	$(5.0 \pm 0.4) \times 10^{-8}$	$(5.6 \pm 0.5) \times 10^{-8}$
m_2	$(1.6 \pm 0.5) \times 10^{-6}$	$(2.1 \pm 0.5) \times 10^{-6}$
s_{2021}	0.526 ± 0.016	0.79 ± 0.03
s_{2022}	0.666 ± 0.018	0.88 ± 0.03
k	0.130	0.126

momentum spread and were also fitted according to Eq. (12). The only difference is that, in this case, the theory [35] suggests a power law with $p_1 = p_2 = 1/2$, which describes the data well. However, the additional scaling factors s_{bt} also had to be applied here. The resulting fit parameters are summarized in Table III.

The beam width is particularly important for an experiment using a vertical cluster beam. As shown in Fig. 6, the target beam has a width on the order of 5 mm. The achieved beam sizes with $\sigma_x < 3$ mm demonstrate that, during the presented measurements, the beam was similar in width to the target or even smaller. This ensures a good overlap of the COSY beam with the target beam and thus high data quality.

VI. BEAM STABILITY STUDIES

In addition to the beam quality studies, studies on the beam stability have been performed. For this purpose, the COSY cycles were extended to roughly 30 min and again different target settings (see Fig. 14) and beam intensities were chosen. The stability of the mean momentum was
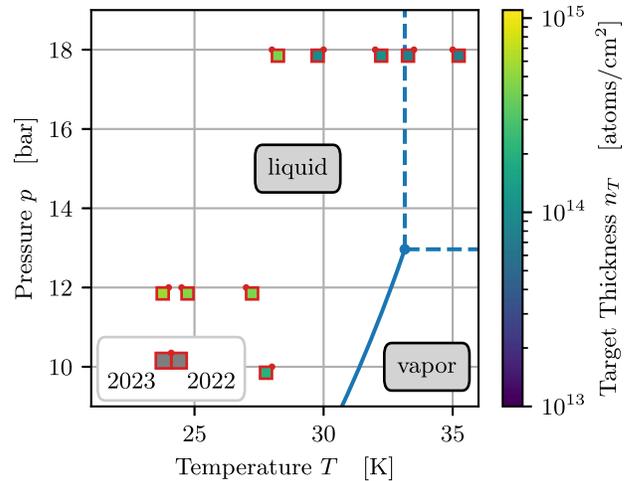

FIG. 14. Target settings with the resulting target thicknesses used during the beam stability measurements in the phase diagram of hydrogen. The solid blue line corresponds to the vapor pressure curve, and the dashed lines mark the region of supercritical hydrogen.
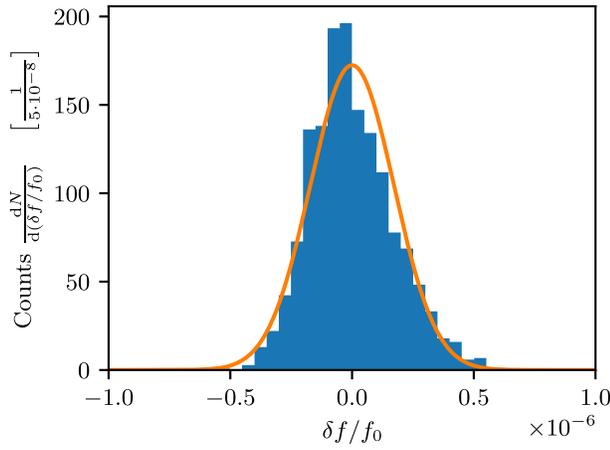
FIG. 15. Histogram showing the relative deviation of the mean frequency of the Schottky spectra from the nominal frequency during a long cycle. The data were recorded with the target operating at 28 K and 18 bar with a target thickness of $(4.4 \pm 0.3) \times 10^{14}$ atoms/cm². The orange line shows a Gaussian with the same center, area, and standard deviation as the histogram.

measured by again taking Schottky spectra every second and now calculating their respective mean, where again only particles inside the bucket are considered and the side peak is neglected. To allow for precooling and to make sure the equilibrium is reached, only data after 5 min in the cycle are considered. Then the standard deviation of the mean momentum from the Schottky spectra within a 25 min time interval is determined, as shown in the histogram in Fig. 15, which is filled with the relative deviations $\delta f/f_0 = (\bar{f} - f_0)/f_0$ from the nominal frequency f_0 of each Schottky spectrum within the considered time interval. This can then also be converted into a momentum stability by using Eq. (8). The resulting stability of the mean momentum for all target settings and beam intensities is summarized in Fig. 16. It can be seen that the stability is below 5×10^{-6}
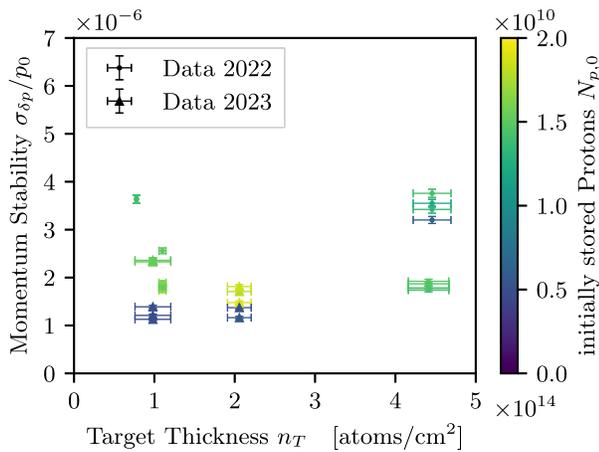

FIG. 16. Momentum stability for different target settings and beam intensities. The initial beam intensity was determined shortly before the target was turned on.

and slightly increases for larger target thickness and beam intensity. It must also be noted that for the data taken at the largest target thickness most of the beam is lost at the end of the cycle, which explains why the mean momentum changes more rapidly. This will be smaller when operating at the HESR with an optimized barrier bucket cavity.

Another study that can be performed with the long cycle data is the evolution of the momentum spread during a cycle when the beam intensity reduces. As already mentioned above, the stochastic cooling requires the gain to be readjusted for every new setting of target thickness and beam intensity in order to achieve the optimum performance. The minimum momentum spread can only be achieved with this optimal gain. However, during a cycle, the beam intensity decreases due to hadronic interactions with the target atoms, so that the stochastic cooling is no longer perfectly adjusted. In this case, the power law with an exponent of $1/3$ is no longer valid. Instead, a linear decrease of the momentum spread is expected [35]. To prove this, the data in the same 25 min interval are divided into 30 s intervals and the momentum spread and beam intensity for each of these intervals are determined and shown in Fig. 17. These data are then fitted with a linear function defined as

$$f(n_T, N_p) = m(N_p - N_{p,0}) + s s_{bt} g(n_T, N_p) \qquad (24)$$

with the slope m and the free scaling parameter s used to scale the fit function from Sec. V multiplied by the beam time scaling factor s_{bt} serve as the starting point for the linear decrease. The scaling parameter is necessary as every cycle might have a slightly different scaling factor due to the
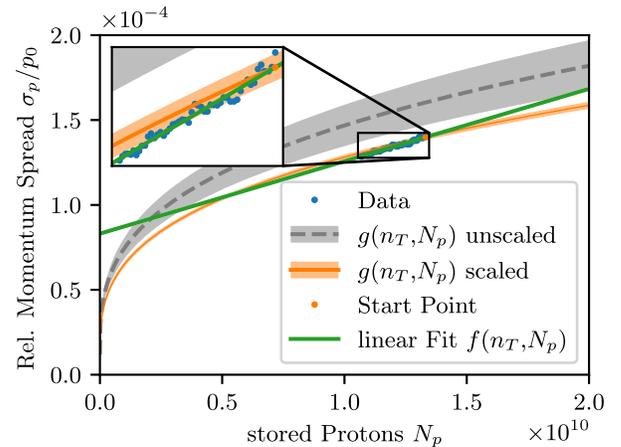

FIG. 17. Momentum spread evolution during a cycle due to the beam intensity reduction recorded with a target thickness of $(4.4 \pm 0.3) \times 10^{14}$ atoms/cm² at 28 K and 18 bar. The fit function from Sec. V is scaled and used as the starting point for a linear function as defined in Eq. (24). The gray error band visualizes the additional uncertainty that reflects the manual adjustment of the stochastic cooling that was introduced with the fit. The orange error band, on the other hand, includes the uncertainties of the fit function and the target thickness.
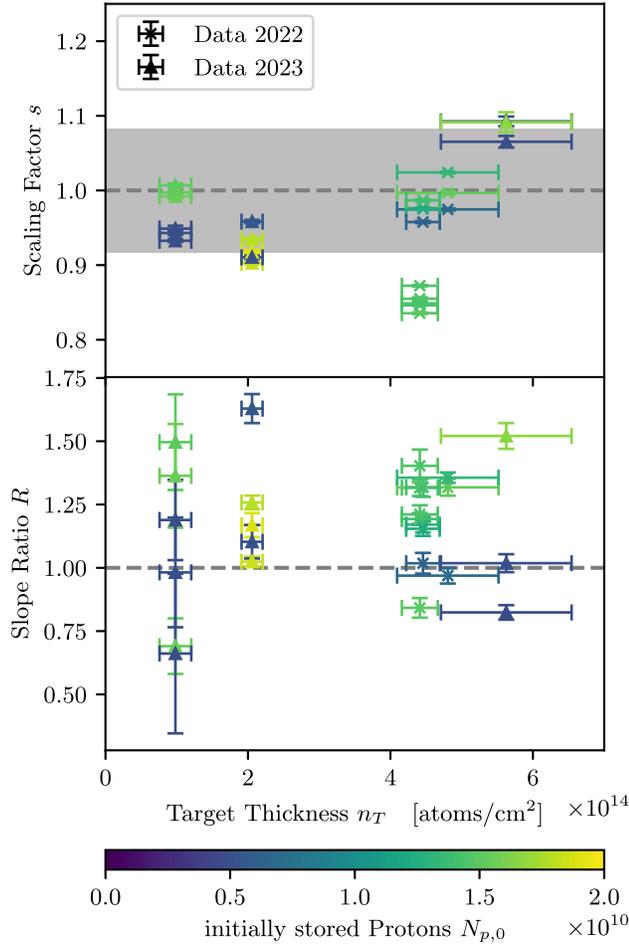
FIG. 18. Results for the linear fit to the momentum spread during a long cycle. Only data with a beam loss of at least 5% are displayed, so that the slope can be determined precisely. Top: scaling parameters to scale the fit function from Sec. V as the starting point of a linear function to the data of the long cycles. The gray error band visualizes the additional uncertainty factor k around the expected scaling factor of 1. Bottom: slope ratio R of the linear fit function to the function $ss_{bt}g(n_T, N_p)$ at the point $(n_T, N_{p,0})$. If the linear function would be a tangent, the value should be 1 as indicated by the dashed line.

manual adjustment of the stochastic cooling. Figure 17 shows that this linear function can describe the data well and better than the function $g(n_T, N_p)$ from the previous section. This is true for all recorded cycles. These measurements prove the theoretical predictions [35] and strengthen the theory of beam-target interaction and stochastic cooling performance.

The results for the free parameters m and s are summarized in Fig. 18. The scaling parameter s reflects the uncertainty of the manual adjustment and should therefore vary around 1 with a variation similar to the uncertainty parameter k from the previous section in Eq. (16). As shown in the upper plot of Fig. 18, the scaling parameter s is indeed close to 1 and mostly varies within the gray error

band that corresponds to the uncertainty factor k. For the slope m, the value should ideally correspond to a tangent to the function $ss_{bt}g(n_T, N_p)$ at the point $(n_T, N_{p,0})$. Therefore, the lower plot shows the slope ratio

$$R = \frac{m}{ss_{bt}g_{N_p}(n_T, N_{p,0})} \quad (25)$$

with the partial derivative $g_{N_p} = \partial g / \partial N_p$. This ratio should be 1 if the function $f(n_T, N_p)$ is a tangent to the function $ss_{bt}g(n_T, N_p)$ at the point $(n_T, N_{p,0})$. The resulting values show significant deviations from the ideal value of 1, although these are less than a factor of 2. This indicates that the cooling was not perfectly adjusted for this initial number of stored protons. However, the perfect adjustment is quite challenging, as the number of stored protons changes from cycle to cycle, and, as shown in Fig. 17, the differences in the momentum spread are only very small.

VII. CONCLUSIONS

This work presents the first results of operating the P̄ANDA cluster-jet target under realistic conditions at the COSY accelerator. The target was operated at different target settings and during the beam times a new record target thickness of $(3.14 \pm 0.17) \times 10^{15}$ atoms/cm^2 was achieved, which has only been exceeded once at the Münster prototype target where the same nozzle was used. Although this very high thickness was only achieved over some hours, it nevertheless shows the potential of the target. A more stable operation is expected as soon as the target will be operated over longer periods of time without long downtimes. At COSY, the target was operated in combination with a pickup and kicker tank of the HESR stochastic cooling and the effect of different target settings and beam intensities has been studied intensely. The results show that the momentum spread can be reduced to values below 2×10^{-4} for all settings, which is already close to the desired values of the P̄ANDA experiment, although the full cooling power is not available at COSY. Furthermore, the dependence of the momentum spread on the target thickness and beam intensity gives important information for the operation at the HESR. Depending on the used model, the target should always be operated at its maximum thickness and only the beam intensity should be adjusted or both should be adjusted simultaneously to reach the optimum momentum spread. Therefore, this study is an important input for the operation of the HESR and the P̄ANDA experiment and it shows how the optimum working conditions can be found. At the HESR, the measurements presented here should be repeated based on the methods discussed within this work to find the best combinations of target thickness and beam intensity for the HESR setup. Therefore, as soon as the HESR, the cluster-jet target, and

the stochastic cooling are ready for operation, the momentum spread and the beam width in the equilibrium should be determined for several combinations of target thickness and beam intensity. These results should then be compared to those found in this work. This can significantly improve the quality of the resonance energy scan program of the P̄ANDA experiment.

Additionally, the beam stability was studied in longer cycles resulting in a relative stability of the mean momentum on the order of 5×10^{-6} or below. This value is partly dominated by the fact that a large fraction of the beam is lost during such a long cycle when operating with a large target thickness and beam intensity. This is a result of the particles that cannot be kept inside the barrier bucket cavity as it was seen in the Schottky spectra by the presence of the side peak. With an optimized barrier bucket cavity at the HESR, the losses will be significantly reduced and by this the stability will be further improved allowing for high quality measurements at P̄ANDA. However, the beam loss at COSY allowed to study the dependence of the momentum spread on the beam intensity without readjusting the stochastic cooling during the cycles. As expected, this can be described better by a linear function than by the power law function with exponents of $p_1 = p_2 = 1/3$. This is an important result as it proves the theory of beam-target interaction and stochastic cooling. Furthermore, it solidifies any theoretical predictions made for the future operation of the stochastic cooling at the HESR.

These studies have proven the feasibility of reaching the high target thickness required by the P̄ANDA experiment while still achieving an excellent beam quality due to the performance of the stochastic cooling and the barrier bucket cavity. This will allow for high quality measurements at the P̄ANDA experiment.

ACKNOWLEDGMENTS

DATA AVAILABILITY

The data that support the findings of this article are openly available [38].

[1] K. Knie, A. Dolinskii, B. Franzke, V. Gostishchev, M. Steck, and P. Sievers, Concept for the antiproton production target at FAIR, in *Proceedings of the International Particle Accelerator Conference, IPAC'12, New Orleans, Louisiana, USA* (JACoW, Geneva, Switzerland, 2012), WEPPD030, https://proceedings.jacow.org/IPAC2012/index.htm.

[2] A. Dolinskii *et al.*, Antiproton complex at the FAIR project, Nucl. Instrum. Methods Phys. Res., Sect. A **629**, 16 (2011).

[3] A. Dolinskii *et al.*, Collector ring project at FAIR, Phys. Scr. **T166**, 014040 (2015).

[4] *FAIR Baseline Technical Report, Volume 2: Accelerator and Scientific Infrastructure*, edited by H. Gutbrod (GSI, Darmstadt, Germany, 2006).

[5] A. Khoukaz *et al.* (P̄ANDA Collaboration), Technical design report for the P̄ANDA internal targets (2012).

[6] H. Stockhorst, D. Prasuhn, R. Maier, B. Lorentz, and T. Katayama, Stochastic cooling for the HESR at the GSI-FAIR complex, in *Proceedings of the European Particle Accelerator conference, EPAC'06, Edinburgh, Scotland* (JACoW, Geneva, Switzerland, 2006), MOPCH086, https://proceedings.jacow.org/e06/INDEX.HTM.

[7] G. Barucca *et al.* (P̄ANDA Collaboration), P̄ANDA phase one, Eur. Phys. J. A **57**, 184 (2021).

[8] S. Navas *et al.* (Particle Data Group), Review of particle physics, Phys. Rev. D **110**, 030001 (2024).

[9] G. Barucca *et al.* (P̄ANDA Collaboration), Precision resonance energy scans with the P̄ANDA experiment at FAIR, Eur. Phys. J. A **55**, 42 (2019).

[10] S. Vestrick, P. Brand, D. Bonaventura, H. Eick, C. Mannweiler, and A. Khoukaz, The Münster cluster-jet target for the future P̄ANDA experiment, EPJ Web Conf. **285**, 02002 (2023).

[11] R. Burgei, M. Garçon, M. Grand, B. Gonel, R. Maillard, A. Mathiery, and J. Martin, A clustered hydrogen gas jet target for the saturne accelerator, Nucl. Instrum. Methods **204**, 53 (1982).

[12] C. Ekström, Internal targets, CAS—CERN Accelerator School: Fourth Advanced Accelerator Physics Course (1992), 10.5170/CERN-1992-001.120.

[13] G. Boero, M. Macri, E. Robutti, D. Allspach, C. Kendziora, and M. Marinelli, The E760 jet target: Measurements of performance at 77-K, Fermi National Accelerator Laboratory (FNAL), Batavia, IL, 1994.

[14] C. Ekström, Internal targets—A review, Nucl. Instrum. Methods Phys. Res., Sect. A **362**, 1 (1995).

[15] H. Dombrowski, D. Grzonka, W. Hamsink, A. Khoukaz, T. Lister, and R. Santo, The Münster cluster target for internal storage ring experiments, Nucl. Instrum. Methods Phys. Res., Sect. A **386**, 228 (1997).

[16] D. Allspach, A. Hahn, C. Kendziora, S. Pordes, G. Boero, G. Garzoglio, M. Macri, M. Marinelli, M. Pallavicini, and E. Robutti, The variable density gas jet internal target for experiment 835 at Fermilab, Nucl. Instrum. Methods Phys. Res., Sect. A **410**, 195 (1998).

[17] A. Täschner, E. Köhler, H.-W. Ortjohann, and A. Khoukaz, High density cluster jet target for storage ring experiments, Nucl. Instrum. Methods Phys. Res., Sect. A **660**, 22 (2011).

[18] H. Dombrowski, D. Grzonka, W. Hamsink, A. Khoukaz, T. Lister, and R. Santo, The Münster cluster target for the COSY-11 experiment, Nucl. Phys. **A626**, 427 (1997).

[19] S. Barsov *et al.*, ANKE, a new facility for medium energy hadron physics at COSY-Jülich, Nucl. Instrum. Methods Phys. Res., Sect. A **462**, 364 (2001).

[20] C. Wilkin, The legacy of the experimental hadron physics programme at COSY, Eur. Phys. J. A **53**, 114 (2017).

[21] S. Vestrick, C. Fischer, and A. Khoukaz, Crossing the Widom line: Cluster formation as sensitive probe of supercritical fluids, J. Supercrit. Fluids **188**, 105686 (2022).

[22] H. Eick, P. Brand, C. Mannweiler, S. Vestrick, A. Khoukaz, D. Schumann, C. Stodel, and M. Gott, Cluster size determination using shadowgraphy measurements, EPJ Web Conf. **285**, 02001 (2023).

[23] S. van der Meer, Stochastic cooling and the accumulation of antiprotons, Rev. Mod. Phys. **57**, 689 (1985).

[24] M. Blaskiewicz and J. M. Brennan, Bunched beam stochastic cooling in a collider, Phys. Rev. ST Accel. Beams **10**, 061001 (2007).

[25] J. Jarvis *et al.*, Optical stochastic cooling experiment at the Fermilab IOTA ring, in *Proceedings of the ABDW-HB'18, Daejeon, Korea* (JACoW, Geneva, Switzerland, 2018), TUP2WA01, 10.18429/JACoW-HB2018-TUP2WA01.

[26] A J. Dick, M. Borland, J. Jarvis, V. Lebedev, P. Piot, A. Romanov, and M. Wallbank, Numerical modeling of a proof-of-principle experiment on optical stochastic cooling at an electron storage ring, Phys. Rev. Accel. Beams **27**, 012801 (2024).

[27] G. Y. Zhu *et al.*, Stochastic cooling experiments for CSRe at IMP, Nucl. Instrum. Methods Phys. Res., Sect. A **932**, 83 (2019).

[28] G. Zhu *et al.*, Stochastic cooling pickup/Kicker developments for the high-precision spectrometer ring in the HIAF project at IMP, IEEE Trans. Nucl. Sci. **68**, 9 (2021).

[29] R. Stassen, B. Breitkreutz, N. Shurkhno, H. Stockhorst, and L. Thorndahl, The HESR stochastic cooling system, design, construction and test experiments in COSY, in *Proceedings of the COOL'17, Bonn, Germany* (JACoW, Geneva, Switzerland, 2018), THA11, 10.18429/JACoW-COOL2017-THA11.

[30] H.-H. Adam *et al.*, Proposal for the wide angle shower apparatus (WASA) at COSY-Jülich—"WASA at COSY", arXiv:nucl-ex/0411038.

[31] A.-K. Hergemöller, Präparation von Clusterstrahlen und der Aufbau der finalen Clusterquelle für das P̄ANDA-experiment, Master's thesis, University of Münster, 2013.

[32] S. Grieser. Cluster-jet targets for the P̄ANDA-, MAGIX-, and CryoFlash-experiments at hadron-, lepton-, and laser-facilities, Doctoral Thesis, University of Münster, 2018.

[33] P. Brand and Universität Münster, The cluster-jet and gas-jet targets for P̄ANDA and MAGIX: upgrades and operation at COSY and MAMI, Ph.D. thesis, Universität Münster, Münster, 2025.

[34] F. Hinterberger, *Beam-Target Interaction and Intrabeam Scattering in the HESR Ring: Emittance, Momentum Resolution and Luminosity* (Forschungszentrum Jülich GmbH, Zentralbibliothek, Jülich, 2006).

[35] H. Stockhorst, T. Katayama, and R. Maier, *Beam Cooling at COSY and HESR Theory and Simulation–Part 1 Theory* (Forschungszentrum Jülich GmbH, Zentralbibliothek, Jülich, 2016).

[36] H. Stockhorst, R. Stassen, D. Prasuhn, R. Maier, T. Katayama, and L. Thorndahl, Stochastic cooling for the HESR at the FAIR facility, in *Proceedings of the Particle Accelerator Conference, PAC'09, Vancouver, British Columbia, Canada* (JACoW, Geneva, Switzerland, 2009), TU6PFP078, https://proceedings.jacow.org/PAC2009/index.htm.

[37] C. Böhme *et al.*, Results of electron cooling beam studies at COSY, in *Proceedings of the RuPAC'10, Protvino, Russia* (JACoW, Geneva, Switzerland, 2010), WECHZ04, https://proceedings.jacow.org/r10/index.htm.

[38] P. Brand, Beam Quality Studies for the Operation of the PANDA Cluster-Jet Target at COSY [Data set], Zenodo, 2025, 10.5281/zenodo.15489475.